J. Fluid Mech. (2013), *vol.* 737, *pp.* 105–131.
doi:10.1017/jfm.2013.564

Receptivity of a supersonic boundary layer to solid particulates

Alexander V. Fedorov†

Department of Aeromechanics and Flight Engineering, Moscow Institute of Physics and Technology, Zhukovski, 140180, Russia

(Received 20 April 2013; revised 8 August 2013; accepted 21 October 2013; first published online 18 November 2013)

Laminar–turbulent transition in the boundary layer at supersonic speeds can be initiated by small solid particles present in the free stream. Particulates interacting with the boundary-layer flow generate unstable wavepackets related to Tollmien–Schlichting (TS) waves. The latter grow downstream and ultimately break down to turbulent spots. This scenario of TS-dominated transition is modelled using the Mack amplitude method. A theoretical model describing the receptivity mechanism is developed to predict the initial spectrum of TS waves. With these initial conditions the downstream growth of TS instability is calculated using the linear stability theory. The transition onset is associated with the point where the disturbance amplitude reaches a threshold value. As an example, calculations are carried out for a 14° half-angle sharp wedge flying in the standard atmosphere at altitude 20 km, Mach number 4 and zero angle of attack. It is shown that spherical particles of radius from 10 to 20 μm and density $\geqslant 1$ g cm^{-3} can cause transition onset corresponding to the amplification factor $N = 9$–10, which is in the empirical range of flight data. This indicates that atmospheric particulates may be a major source of TS-dominated transition on aerodynamically smooth surfaces at supersonic speeds. The receptivity model provides a foundation for further treatments of different cases associated with transition in dusty environments. It can also be used for predictions of particle-induced transition at subsonic and hypersonic speeds.

Key words: boundary layer receptivity, boundary layer stability, transition to turbulence

1. Introduction

Laminar–turbulent transition is a multiphase process which is initiated by the ambient disturbance environment (Reshotko 1976; Morkovin, Reshotko & Herbert 1994). External disturbances, which can be stream-generated and/or body-generated, interact with the mean-flow field and constitute the initial values for the boundary-layer instabilities. This receptivity mechanism provides the initial conditions for the subsequent linear and nonlinear phases which ultimately lead to final breakdown to turbulence. Under 'quiet' free-stream conditions, the transition onset is usually predicted using the e^N method (for example, Jaffe, Okamura & Smith 1970; Hefner & Bushnell 1979; Malik 1990, 1997) which deals with the amplification ratio given by the linear stability theory. This semi-empirical method can only estimate the transition

† Email address for correspondence: fedorov@falt.ru

onset for a certain class of bodies and external disturbances. To improve prediction accuracy and treat non-canonical configurations and disturbance fields, one should solve an initial boundary-value problem which requires detailed specification of the ambient disturbance environment.

This motivated Bushnell (1990) to summarize information concerning the qualitative nature of the initial disturbances for atmospheric flights. He pointed out that, along with roughness, stream turbulence, acoustic radiation from the vehicle itself and electrostatic discharges, solid particulates can be a major source of disturbance energy. Particulates can affect transition via different mechanisms (Bushnell 1990): (i) impacting/striking on the surface leading to surface 'cratering'; (ii) vortex/vorticity shedding while the particle is immersed in the boundary layer; (iii) particle rotation and consequent fluid motions; (iv) production of 'reverse shocklets' after passage through the vehicle-induced shock; (v) rebound after impact on the vehicle surface and subsequent dynamic interaction with the bow shock causing formation of embedded shear layers and jets.

Although particles are present in all test environments (unless special filtering techniques are employed), the particulate matter is better documented for the atmosphere than for the experimental ground facilities. The occurrence of atmospheric particles is associated with ice clouds, volcanic and other terrestrial dust as well as cosmic dust (for example, Turco 1992; Deepak *et al.* 1999). Of particular interest is a finding that a substantial portion of particles of size 10 μm or greater consists of the products of rocket exhausts from previous flights (Bushnell 1990).

Particle-induced transition has received considerable attention for incompressible boundary layers. Chen, Goland & Reshotko (1980) suspected that particulates in the environment of underwater vehicles may be responsible for the generation of turbulent patches in the laminar boundary layer of the vehicle. This speculation was examined through an attempt at calculating the turbulent patch generation rate with the assumption that patches are induced by sufficiently large particles. Lauchle, Pertie & Stinebring (1995) examined experimentally the effects of small uniformly sized spherical particles seeded into the free stream of a water tunnel on transition in the boundary layer on a heated laminar-flow-control body. It was shown that the transition Reynolds number (based on the body arclength and the approach flow velocity) decreases monotonically with increase in the ratio of the particle diameter to the displacement thickness. Ladd & Hendricks (1985) also observed transition on an axisymmetric heated body under the influence of freely suspended particles. They estimated a critical particle Reynolds number, $Re_{dc} = (u^* d^*/\nu^*)_c$, where d^* is particle diameter, ν^* is kinematic viscosity, and u^* is the local velocity in the boundary layer at a distance d^* from the wall at the locations where turbulent spots were formed. The values of this Reynolds number fall within a range of 400–700 which is similar to that observed for spherical particles fixed to the wall (Smith & Clutter 1959; Hall 1967).

The effects of an isolated, stationary spherical particle on the transition process in the boundary layer on a flat plate were examined by Saiki & Bringen (1996) using a spatial direct numerical simulation (DNS). It was found that a particle of subcritical diameter induces hairpin vortices, which decay as they are convected downstream. In the supercritical case, an isolated disturbance rapidly breaks down and forms a structure resembling a turbulent spot. The DNS results correlate with the experimental observations of Blackwelder *et al.* (1992). They examined the influence of a moving sphere with a diameter of roughly 1/3 the boundary-layer thickness. Taniguchi, Browand & Blackwelder (2000) studied experimentally (in a water channel) and numerically transition induced by a single heavy spherical particle free-falling

through a laminar boundary layer on a flat plate. The experiment showed that the wake left by the falling particle was capable of triggering a turbulent spot. The DNS revealed that the particle-induced wake behaves as a Hill's spherical vortex causing transition under certain conditions.

To our knowledge, particle effects on transition in high-speed flows have not been studied in any great detail. Holden (1975) performed experiments on a flat-ended cylinder in a hypersonic free stream at Mach number 6 and 13. These experiments are related to the particle rebound after impact on the blunt-body nose at hypersonic speeds. Holden studied the generation of disturbances in the stagnation region as a particle, which is launched upstream from the model surface, interacts with the bow shock. It was found that there was a small heating enhancement near the stagnation point as the particle (between 100 and 800 μm in size) passed through the shock layer. However heating levels between 3 and 10 times the stagnation-point value were generated as the particle penetrates the bow shock. When a particle penetrates more than the body diameter beyond the bow shock, massive flow instabilities similar to those encountered over spiked bodies were observed. Presumably, these instabilities can trigger premature transition on the body surface.

The foregoing studies were predominantly focused on relatively large particles enabling the bypass mechanism to be triggered. However in many practical cases the particle size is quite small. For example, the diameter of stratospheric particulates is, typically, of the order of 10 μm or less. Such minute particles cannot trigger turbulent patches, while they can generate the boundary-layer instabilities of small initial amplitudes via a receptivity mechanism, which has not been studied yet. This motivated us to conduct a theoretical analysis of a unit problem describing excitation of the boundary-layer modes by spherical solid particles interacting with the boundary-layer flow on a body moving with a supersonic speed. The analysis is focused on the dynamic interaction of particles with the boundary-layer flow. Effects associated with particle-induced vortical disturbances, acoustic waves and roughness are not considered. Solutions of this problem are incorporated into the amplitude method of Mack (1977) to estimate the particle-induced transition onset.

The paper is organized as follows. In § 2 we consider the dynamics of spherical solid particles penetrating into the boundary layer. In § 3 we formulate and solve the receptivity problem describing excitation of an unstable wavepacket by a small particle crossing the boundary layer. The downstream evolution of this wavepacket is analysed using the steepest descent method in the framework of local-parallel linear stability theory. The threshold amplitude related to the transition onset is estimated using available experimental and numerical data. In § 4 we consider the particle-induced transition on a sharp wedge at free-stream Mach number 4. In this case, transition is associated with instability of the first mode (Mack 1969). Because this mode is an extension to high speeds of the Tollmien–Schlichting (TS) waves, hereafter we call it a TS mode. The TS-dominated transition onset is estimated for particulates of various size and density. The results are summarized in § 5.

2. Particle dynamics

Consider a laminar flow past a body in a supersonic free stream of speed U_1^*, density ρ_1^* and temperature T_1^* (figure 1). Herein asterisks denote dimensional quantities. The inviscid shock layer between the bow shock and the body surface is assumed to be much thicker than the viscous boundary layer, i.e. the Reynolds number (based on the free-stream parameters and the body length) is large. In the shock layer,

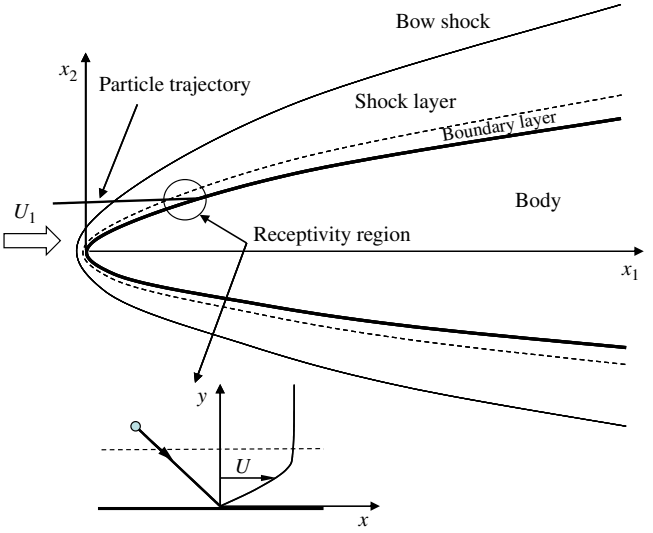

FIGURE 1. Schematic of a supersonic flow past the body surface and the coordinate systems.

the flow has velocity $\boldsymbol{u}^*(\boldsymbol{x}^*)$, density $\rho^*(\boldsymbol{x}^*)$, temperature $T^*(\boldsymbol{x}^*)$ and pressure $P^*(\boldsymbol{x}^*)$, where $\boldsymbol{x}^* = (x_1^*, x_2^*, x_3^*)^{\mathrm{T}}$. At the initial time instant $t^* = t_0^*$, a solid spherical particle of density ρ_p^* and radius r_p^* crosses the shock at a point $\boldsymbol{x}^* = \boldsymbol{x}_0^*$. Since the particle cannot immediately slow down, its initial velocity just behind the shock is $\boldsymbol{u}_p^*(t_0^*) = (U_1^*, 0, 0)^{\mathrm{T}}$. In the shock layer, the particle dynamics is governed by the equations

$$m^* \frac{\mathrm{d}\boldsymbol{u}_p^*}{\mathrm{d}t^*} = \boldsymbol{F}_p^*, \tag{2.1}$$

$$\boldsymbol{u}_p^*(t_0^*) = (U_1^*, 0, 0)^{\mathrm{T}}, \tag{2.2}$$

where $m^* = 4\pi r_p^{*3}\rho_p^*/3$ is the particle mass and $\boldsymbol{F}_p^*$ is the drag force. The gravitational force on the particle is assumed to be negligible in comparison with the aerodynamic drag. It is assumed that the hydrodynamic time scale r_p^*/u_0^*, where $u_0^* = |\boldsymbol{u}_p^* - \boldsymbol{u}^*|_{t^*=t_0^*}$ is the initial relative velocity of the particle, is much shorter than the particle deceleration time scale $m^* u_0^*/F_p^*$. Then the flow past the particle is treated as quasi-steady, and the drag is calculated as

$$\boldsymbol{F}_p^* = -C_D \frac{\rho^*}{2} |\boldsymbol{u}_p^* - \boldsymbol{u}^*|(\boldsymbol{u}_p^* - \boldsymbol{u}^*)\pi r_p^{*2}. \tag{2.3}$$

This approximation is valid for $\rho_p^* \gg C_D\rho^*$ that is typical for dust particles in air flows. Hence the particle trajectory $\boldsymbol{x}_p^*(t^*)$ and velocity $\boldsymbol{u}_p^*(t^*)$ are solutions of the problem

$$\frac{\mathrm{d}\boldsymbol{x}_p^*}{\mathrm{d}t^*} = \boldsymbol{u}_p^*, \tag{2.4}$$

$$\frac{\mathrm{d}\boldsymbol{u}_p^*}{\mathrm{d}t^*} = \frac{3}{8} C_D \frac{\rho^*}{\rho_p^*} \frac{|\boldsymbol{u}_p^* - \boldsymbol{u}^*|(\boldsymbol{u}^* - \boldsymbol{u}_p^*)}{r_p^*}, \tag{2.5}$$

$$\boldsymbol{x}_p^*(t_0^*) = \boldsymbol{x}_0^*, \tag{2.6}$$

$$\boldsymbol{u}_p^*(t_0^*) = (U_1^*, 0, 0)^{\mathrm{T}}. \tag{2.7}$$

If the particle radius is much smaller than the boundary-layer thickness in the vicinity of the particle impact on the body surface, $r_p^* \ll \delta^*$, then the problem (2.4)–(2.7) describes the particle passage through the viscous boundary layer also.

For spherical particles the drag coefficient can be calculated using the empirical correlations of Crowe (1967) and Henderson (1976)

$$C_D = fn(Re_p, M_p, T_p^*/T^*), \tag{2.8}$$

where $Re_p = 2r_p^*\rho^*|\boldsymbol{u}_p^* - \boldsymbol{u}^*|/\mu^*$ is relative Reynolds number, $M_p = |\boldsymbol{u}_p^* - \boldsymbol{u}^*|/a^*$ is relative Mach number, and T_p^* is temperature of the particle surface. The correlation of Crowe (1967) has been developed for the ranges $0.2 < Re_p < 10^4$ and $0.1 < M_p < 2$. For higher Mach numbers, it is recommended to use the correlation of Henderson (1976) valid up to $M_p = 6$. Hereafter we use the correlation of Crowe (1967).

Analysing (2.5) we introduce a relaxation time $\tau^* = (8/3)(\rho_p^*/\rho^*)(r_p^*/C_{D0}u_0^*)$ and a generalized Stokes number $St = l^*u_0^*/\tau^*$, where l^* is a characteristic thickness of the shock layer. Depending on the Stokes number the following typical cases can be identified.

In case 1 for $St \gg 1$, the drag force is so small that the particle moves to the wall with approximately constant speed $\boldsymbol{u}_p^* = (U_1^*, 0, 0)^{\mathrm{T}}$. In the leading-order approximation, the particle trajectory is a straight line $\boldsymbol{x}_p^*(t^*) = \boldsymbol{x}_0^* + (U_1^*, 0, 0)^{\mathrm{T}}t^*$.

In case 2 for $St \sim 1$ and $l^* \gg \delta^*$, the particle momentum loss is appreciable in the inviscid shock layer while it is negligible in the relatively thin viscous boundary layer. By solving the problem (2.4)–(2.7) in the shock layer, we can determine the particle velocity $\boldsymbol{u}_{pw}^*$ at the impact and assume that the particle passes through the boundary layer with constant speed $\boldsymbol{u}_{pw}^*$. Note that case 2 contains case 1.

In case 3 for $St \ll 1$, the particle is quickly slowed down in the bow-shock vicinity and it does not reach the boundary layer. During this deceleration the particle generates acoustic disturbances (shocklets), which propagate to the wall and interact with the boundary layer. Such relatively light and/or small particles form a 'noisy' layer just behind the shock.

Hereafter we focus on cases 1 and 2 where particles cross the boundary layer and reach the body surface. Note that in the case of $l^* \sim \delta^*$ related to a viscous shock layer, the receptivity problem should be formulated without distinction between viscous and inviscid mean flows. However this case corresponds to very high free-stream Mach numbers and/or relatively small Reynolds numbers at which the laminar flow is, as a rule, stable and transition does not occur.

3. Receptivity problem and prediction of the transition onset

Consider case 2 (see § 2) where the particle passes through a relatively thin boundary layer with approximately constant speed $\boldsymbol{u}_{pw}^*$. The latter is a solution of the dynamic equations (2.4)–(2.7) in the inviscid shock layer. For simplicity, the particle is not reflected from the wall. The effects related to the particle-induced roughness or particle rebound are not considered.

If the bow-shock angle is not small, the angle between the velocity vector $\boldsymbol{u}_{pw}^*$ and the body surface is $O(1)$. Then the particle trajectory within the boundary layer lies in a region Δx^* which is of the order of the local boundary-layer thickness δ^*. The particle radius is assumed to be much smaller than δ^*. The particle generates flow disturbances (including unstable modes) in a local region where the unperturbed

laminar boundary-layer flow can be treated as parallel. Further analysis is focused on this receptivity region schematically shown in figure 1.

3.1. *Governing equations*

A small particle induces a concentrated force and a heat source (if the particle surface is not adiabatic). The flow field in the receptivity region is governed by the Navier–Stokes equations written in dimensionless form

$$\frac{\partial \rho}{\partial t} + \frac{\partial}{\partial x_j}(\rho u_j) = 0, \tag{3.1}$$

$$\frac{\partial}{\partial t}(\rho u_i) + \frac{\partial}{\partial x_j}(\rho u_i u_j + p\delta_{ij}) = \frac{1}{R}\frac{\partial \tau_{ij}}{\partial x_j} + r_p^2 \bar{F}_{pi}\delta(\boldsymbol{x} - \boldsymbol{x}_p), \tag{3.2}$$

$$\rho\left[\frac{\partial T}{\partial t} + u_j\frac{\partial T}{\partial x_j}\right] = \frac{1}{PrR}\frac{\partial}{\partial x_j}\left(\mu\frac{\partial T}{\partial x_j}\right) + (\gamma - 1)M_e^2\left(\frac{\partial p}{\partial t} + u_j\frac{\partial p}{\partial x_j}\right) + \frac{(\gamma - 1)M_e^2}{R}\Phi + \frac{r_p}{PrR}\bar{Q}_p\delta(\boldsymbol{x} - \boldsymbol{x}_p) + r_p^2(\gamma - 1)M_e^2(u_{pj} - u_j)\bar{F}_{pj}\delta(\boldsymbol{x} - \boldsymbol{x}_p), \tag{3.3}$$

$$\gamma M_e^2 p = \rho T, \tag{3.4}$$

where the velocity components, density, temperature and pressure are scaled using their quantities U_e^*, ρ_e^*, T_e^* and $\rho_e^* U_e^{*2}$ at the upper boundary-layer edge τ_{ij} is the shear stress, δ_{ij} is the Kronecker symbol, γ is specific heat ratio, Pr is Prandtl number and μ is dynamic viscosity. The length scale Δ^* is of the order of the boundary-layer thickness, the time scale is Δ^*/U_e^*, the Reynolds number is $R = \rho_e^* U_e^* \Delta^*/\mu_e^*$, and the local Mach number is M_e. The momentum equation (3.2) contains the particle-induced force components $r_p^2 \bar{F}_{pi}\delta(\boldsymbol{x} - \boldsymbol{x}_p)$, where $\delta(\boldsymbol{x} - \boldsymbol{x}_p) = \delta(x_1 - x_{p1})\delta(x_2 - x_{p2})\delta(x_3 - x_{p3})$ is delta function,

$$\bar{F}_{pi} = C_D\frac{\rho}{2}|\boldsymbol{u} - \boldsymbol{u}_p|(u_{ip} - u_i)\pi, \tag{3.5}$$

$r_p = r_p^*/\Delta^*$ is a small parameter characterizing the particle size relative to the boundary-layer thickness near the location of particle impact. The energy equation (3.3) contains the dissipation function Φ, the particle-induced energy source proportional to $\bar{Q}_p = 2\pi Nu(T_p - T)$, where Nu is the Nusselt number, as well as the power source term proportional to $(u_{pj} - u_j)\bar{F}_{pj}$.

3.2. *Receptivity analysis*

Introduce a local coordinate system (x, y, z), in which the particle impact point is $(0, 0, 0)$ and the impact occurs at the time instant $t = 0$. Because $r_p \ll 1$, the flow field quantities can be expressed as

$$q(x, y, z, t) = Q(x, y, z) + r_p^2\tilde{q}(x, y, z, t), \tag{3.6}$$

where q denotes an arbitrary flow variable. In the first-order approximation with respect to r_p^2, the particle-induced disturbance $(\tilde{\rho}, \tilde{u}, \tilde{v}, \tilde{w}, \tilde{p}, \tilde{T})$ is governed by the linearized Navier–Stokes equations. In the receptivity region schematically shown in figure 1, the basic flow parameters are approximated as

$$\left.\begin{aligned} &U = U_s(X, y) + O(\varepsilon), \quad V = \varepsilon\, V_0(X, y) + O(\varepsilon^2), \\ &W = W_s(X, y) + O(\varepsilon), \quad P = P_s(X) + O(\varepsilon^2), \quad T = T_s(X, y) + O(\varepsilon), \end{aligned}\right\} \tag{3.7}$$

where $\varepsilon = R^{-1} \ll 1$, and $X = \varepsilon x$ is a slow variable. Hereafter the particle velocity components are (U_p, V_p, W_p). The disturbance field is expressed in the vector form

$$\boldsymbol{\Psi}(x, y, z, t) = \left(\tilde{u}, \frac{\partial \tilde{u}}{\partial y}, \tilde{v}, \tilde{p}, \tilde{T}, \frac{\partial \tilde{T}}{\partial y}, \tilde{w}, \frac{\partial \tilde{w}}{\partial y}\right)^{\mathrm{T}}. \tag{3.8}$$

Because the basic flow does not depend on x and z in the leading-order approximation with respect to ε, we can perform Fourier transforms for these variables

$$\boldsymbol{\psi}(y, t; \alpha, \beta) = \int_{-\infty}^{+\infty} \int_{-\infty}^{+\infty} \boldsymbol{\Psi}(x, y, z, t) \exp(-\mathrm{i}\alpha x - \mathrm{i}\beta z)\, \mathrm{d}x\, \mathrm{d}z. \tag{3.9}$$

The amplitude function $\boldsymbol{\psi}(y, t; \alpha, \beta)$ is governed by a system of linear equations, which can be written in the matrix-operator form

$$\boldsymbol{H}_1 \frac{\partial \boldsymbol{\psi}}{\partial t} + \boldsymbol{H}_2(y, \partial_y, \alpha, \beta)\boldsymbol{\psi} = \boldsymbol{G}. \tag{3.10}$$

Here the vector $\boldsymbol{G}(t, y)$ contains Fourier components of the particle-induced source terms

$$\boldsymbol{G}(t, y) = \boldsymbol{g}(x_p, y, z_p)\delta(y - y_p) \exp(-\mathrm{i}\alpha x_p - \mathrm{i}\beta z_p), \tag{3.11}$$

the vector $\boldsymbol{g}$ is given in the Appendix, and $x_p(t)$, $y_p(t)$ and $z_p(t)$ are coordinates of the particle trajectory. The boundary conditions are formulated as

$$y = 0 : (\psi_1, \psi_3, \psi_5, \psi_7) = 0, \tag{3.12}$$

$$y \to \infty : |\boldsymbol{\psi}| < \infty, \tag{3.13}$$

$$t \to -\infty : \boldsymbol{\psi}(y, t) \to 0. \tag{3.14}$$

The condition (3.12) implies that the disturbance field has zero velocity and temperature on the body surface. The condition (3.14) implies that there are no disturbances when the particle is far from the boundary layer.

The problem (3.10)–(3.14) can be solved using the biorthogonal eigenfunction decomposition method (Zhigulev & Tumin 1987). A biorthogonal eigenfunction system was formulated by Salwen & Grosch (1981) with respect to a temporal stability problem for incompressible boundary-layer flow. Tumin & Fedorov (1983) extended this analysis to the case of a compressible boundary layer. This method was further developed by Fedorov & Tumin (2003) and Tumin (2007).

Following Fedorov & Tumin (2003) we introduce the eigenfunction system $\{\boldsymbol{A}(y; \alpha, \beta, \omega), \boldsymbol{B}(y; \alpha, \beta, \omega)\}$, where $\boldsymbol{A}$ is a solution of the direct homogeneous problem

$$-\mathrm{i}\omega \boldsymbol{H}_1 \boldsymbol{A} + \boldsymbol{H}_2(y, \partial_y, \alpha, \beta)\boldsymbol{A} = 0, \tag{3.15}$$

$$y = 0 : (A_1, A_3, A_5, A_7) = 0, \tag{3.16}$$

$$y \to \infty : |\boldsymbol{A}| < \infty, \tag{3.17}$$

and $\boldsymbol{B}$ is a solution of the adjoint problem

$$\mathrm{i}\bar{\omega} \boldsymbol{H}_1^* \boldsymbol{B} + \boldsymbol{H}_2^*(y, \partial_y, \alpha, \beta)\boldsymbol{B} = 0, \tag{3.18}$$

$$y = 0 : (B_2, B_4, B_6, B_8) = 0, \tag{3.19}$$

$$y \to \infty : |\boldsymbol{B}| < \infty. \tag{3.20}$$

Here the asterisk denotes a Hermitian adjoint matrix, the overbar denotes a complex conjugate value, and the frequency ω is a complex eigenvalue. The eigenfunctions

satisfy to the orthogonality condition

$$\langle \boldsymbol{H}_1\boldsymbol{A}(y;\alpha,\beta,\omega), \boldsymbol{B}(y;\alpha,\beta,\omega')\rangle \equiv \int_0^\infty (\boldsymbol{H}_1\boldsymbol{A}(y;\alpha,\beta,\omega)\cdot\boldsymbol{B}(y;\alpha,\beta,\omega'))\,\mathrm{d}y = \Delta_{\omega\omega'}, \tag{3.21}$$

where $\Delta_{\omega\omega'} = \delta_{nm}$ is the Kronecker symbol if ω and ω' belong to modes n and m of the discrete spectrum, and $\Delta_{\omega\omega'} = \delta(\omega-\omega')$ is a delta function if both ω and ω' belong to the continuous spectrum. Equation (3.15) can be written in the form (see, for example, Mack 1969 and Nayfeh 1980)

$$\left(\frac{\partial}{\partial y} - \boldsymbol{H}_0\right)\boldsymbol{A} = 0, \tag{3.22}$$

where $\boldsymbol{H}_0$ is a standard matrix of the linear stability problem. Its non-zero elements are given in the Appendix. The matrix $\boldsymbol{H}_1$ is expressed in terms of $\boldsymbol{H}_0$

$$\boldsymbol{H}_1 = \mathrm{i}\frac{\partial \boldsymbol{H}_0}{\partial\omega}. \tag{3.23}$$

A solution of the problem (3.10)–(3.14) is decomposed as

$$\begin{aligned}\boldsymbol{\psi}(t,y) = &\sum_n C_n(t)\boldsymbol{A}_n(y;\alpha,\beta)\exp(-\mathrm{i}\omega_n(\alpha,\beta)t)\\ &+\sum_j\int_0^\infty C_j(t,k)\boldsymbol{A}_j(y;\alpha,\beta,k)\exp(-\mathrm{i}\omega_j(\alpha,\beta,k)t)\,\mathrm{d}k.\end{aligned} \tag{3.24}$$

Here the first sum contains normal modes of the discrete spectrum $\omega_n(\alpha,\beta)$ including unstable modes. The second sum contains integrals over branches of the continuous spectrum including fast and slow acoustic waves as well as vorticity and entropy waves. These integrals form shocklets and entropy/vorticity wakes induced by the particle. Further analysis is focused on the excitation of one unstable mode of the discrete spectrum (say mode m with the eigenvalue $\omega_m(\alpha,\beta)$ and the eigenfunction $\boldsymbol{A}_m$). Substituting (3.24) into (3.10) and multiplying by $\boldsymbol{B}_m(y,\alpha,\beta)$, we obtain the ordinary differential equation for the weight coefficient $C_m(t)$

$$\mathrm{i}\left\langle\frac{\partial\boldsymbol{H}_0}{\partial\omega}\boldsymbol{A}_m,\boldsymbol{B}_m\right\rangle\frac{\mathrm{d}C_m}{\mathrm{d}t} = \langle\boldsymbol{G},\boldsymbol{B}_m\rangle\mathrm{e}^{\mathrm{i}\omega_m t} \tag{3.25}$$

with the boundary condition

$$C_m(-\infty) = 0. \tag{3.26}$$

Substituting (3.11) into (3.25) and integrating over time, we get

$$C_m = -\mathrm{i}\left\langle\frac{\partial\boldsymbol{H}_0}{\partial\omega}\boldsymbol{A}_m,\boldsymbol{B}_m\right\rangle^{-1}\int_{-\infty}^{t}(\boldsymbol{g},\boldsymbol{B}_m)_{y=y_p}\exp(\mathrm{i}\omega_m t - \mathrm{i}\alpha x_p - \mathrm{i}\beta z_p)\,\mathrm{d}t. \tag{3.27}$$

If the particle-induced roughness is neglected, then $\boldsymbol{g}(t) = 0$ for $t > 0$ (after the impact), and the weight coefficient attains a constant value which is calculated using (3.27) with the upper limit of integration $t = 0$. The inverse Fourier transforms give the particle-induced wavepacket related to mode m

$$\begin{aligned}&t>0:\ \boldsymbol{\Psi}_m(x,y,z,t)\\ &\quad=\frac{1}{(2\pi)^2}\int_{-\infty}^{+\infty}\int_{-\infty}^{+\infty}C_m(\alpha,\beta)\boldsymbol{A}_m(y;\alpha,\beta)\exp(\mathrm{i}\alpha x+\mathrm{i}\beta z-\mathrm{i}\omega_m t)\,\mathrm{d}\alpha\,\mathrm{d}\beta.\end{aligned} \tag{3.28}$$

The foregoing analysis has been conducted using the eigenfunctions of the temporal problem, where α and β are real and $\omega_m(\alpha, \beta)$ is a complex eigenvalue. Because the instabilities considered herein are convective, they grow in space rather than amplify in time. For the cases where the basic flow does not depend on z, the temporally evolving wavepacket (3.28) can be converted into a spatially evolving one. Consider the integral

$$I = \int_{-\infty}^{+\infty} C_m(\alpha, \beta)\boldsymbol{A}_m(y; \alpha, \beta) \exp(\mathrm{i}\alpha x + \mathrm{i}\beta z - \mathrm{i}\omega_m t)\, \mathrm{d}\alpha, \tag{3.29}$$

which includes the waves of fixed β. With the substitution $\mathrm{d}\alpha = (\partial\omega_m/\partial\alpha)^{-1}\,\mathrm{d}\omega$, this integral is written as

$$I = \int_{\gamma_m} \left(\frac{\partial\omega_m}{\partial\alpha}\right)^{-1} C_m(\omega, \beta)\boldsymbol{A}_m(y; \omega, \beta) \exp(\mathrm{i}\alpha_m x + \mathrm{i}\beta z - \mathrm{i}\omega t)\, \mathrm{d}\omega, \tag{3.30}$$

where $\alpha_m(\omega)$ maps a certain interval of the contour γ_m into an interval of real α. If this mapping is not singular and $\partial\omega_{mr}/\partial\alpha > 0$ everywhere (waves propagate downstream), we can displace the contour γ_m to the real axis of the complex-ω-plane and obtain

$$I = \int_{-\infty}^{+\infty} \left(\frac{\partial\alpha_m}{\partial\omega}\right) C_m(\omega, \beta)\boldsymbol{A}_m(y; \omega, \beta) \exp(\mathrm{i}\alpha_m x + \mathrm{i}\beta z - \mathrm{i}\omega t)\, \mathrm{d}\omega. \tag{3.31}$$

Hereafter the subscript 'r' ('i') denotes the real (imaginary) part of a complex quantity. Substituting (3.31) into (3.28) and using the relationship

$$\frac{\partial\alpha_m}{\partial\omega} = -\left\langle \frac{\partial\boldsymbol{H}_0}{\partial\omega}\boldsymbol{A}_m, \boldsymbol{B}_m \right\rangle \Big/ \left\langle \frac{\partial\boldsymbol{H}_0}{\partial\alpha}\boldsymbol{A}_m, \boldsymbol{B}_m \right\rangle, \tag{3.32}$$

we get the spatially evolving wavepacket

$$x > 0: \boldsymbol{\Psi}_m(x, y, z, t) = \frac{1}{(2\pi)^2} \int_{-\infty}^{+\infty}\int_{-\infty}^{+\infty} D_m(\omega, \beta)\boldsymbol{A}_m(y; \omega, \beta) \times \exp(\mathrm{i}\alpha_m x + \mathrm{i}\beta z - \mathrm{i}\omega t)\, \mathrm{d}\omega\, \mathrm{d}\beta, \tag{3.33}$$

$$D_m = \mathrm{i}\left\langle \frac{\partial\boldsymbol{H}_0}{\partial\alpha}\boldsymbol{A}_m, \boldsymbol{B}_m \right\rangle^{-1} \int_{-\infty}^{0} (\boldsymbol{g}, \boldsymbol{B}_m)_{y=y_p} \exp(\mathrm{i}\omega t - \mathrm{i}\alpha_m x_p - \mathrm{i}\beta z_p)\, \mathrm{d}t. \tag{3.34}$$

Note that the solution (3.33)–(3.34) can be obtained from the analysis of the spatial problem using the technique developed by Fedorov & Khokhlov (2002).

If the particles cross the boundary layer with a constant speed $(U_p, V_p, 0)$, the weight coefficient (3.34) can be expressed as

$$D_m = \mathrm{i}\left\langle \frac{\partial\boldsymbol{H}_0}{\partial\alpha}\boldsymbol{A}_m, \boldsymbol{B}_m \right\rangle^{-1} \int_{+\infty}^{0} \varphi_m(y)\, \mathrm{d}y, \tag{3.35}$$

$$\varphi_m(y) = \frac{(\boldsymbol{g}, \boldsymbol{B}_m)}{V_p} \exp\left(-\mathrm{i}\alpha_m y \frac{U_p - c_m}{V_p}\right), \tag{3.36}$$

where $c_m = \omega/\alpha_m$ is the complex phase speed. The complex function $\varphi_m(y)$ characterizes a local contribution of the particle-induced source to the instability amplitude. The relations (3.35) and (3.36) correspond to the case of two-dimensional mean flow where the lateral coordinate of a spherical particle does not change, $z_p(t) = 0$. They are used for the numerical examples of § 4.

3.3. *Unstable wavepackets and transition onset*

Accounting for slow variations of the wavepacket characteristics due to the downstream growth of the boundary-layer thickness, we can write (3.33) in the WKB form

$$x \gg x_0 : \boldsymbol{\Psi}_m = \frac{1}{(2\pi)^2} \int_{-\infty}^{\infty} \int_{-\infty}^{\infty} D_m(\omega, \beta) \boldsymbol{A}_m(x, y, \beta, \omega) \times \exp(\mathrm{i}S + \mathrm{i}\beta z - \mathrm{i}\omega t)\, \mathrm{d}\omega\, \mathrm{d}\beta, \tag{3.37}$$

$$S = \int_{x_0}^{x} \alpha_m(x, \beta, \omega)\, \mathrm{d}x, \tag{3.38}$$

where the longitudinal coordinate x is measured along the body surface from the body leading edge, and the particle impact occurs at the point $(x, y, z) = (x_0, 0, 0)$.

If the particle strike is far upstream from the final point where the instability is evaluated ($x \gg x_0$), then the integrals over ω and β can be estimated using the steepest descent method

$$\boldsymbol{\Psi}_m \approx \frac{2}{\pi} \mathrm{Re}[\mathrm{i}K(\omega_s, \beta_s) D_m(\omega_s, \beta_s) \boldsymbol{A}_m(x, y, \beta_s, \omega_s) \exp(\mathrm{i}S(\omega_s, \beta_s) + \mathrm{i}\beta_s z_s - \mathrm{i}\omega_s t_s)], \tag{3.39}$$

$$K = \left[\frac{\partial^2 S}{\partial \omega^2} \frac{\partial^2 S}{\partial \beta^2} - \left(\frac{\partial^2 S}{\partial \omega \partial \beta} \right)^2 \right]^{-1/2}, \tag{3.40}$$

where ω_s, β_s are determined from the relations

$$\frac{\partial S_i}{\partial \omega} = 0, \quad \frac{\partial S_i}{\partial \beta} = 0. \tag{3.41}$$

The coordinate z_s and time t_s, are related to the disturbance maximum. They are determined from the equations

$$\frac{\partial S_r}{\partial \omega} - t = 0, \quad \frac{\partial S_r}{\partial \beta} - z = 0. \tag{3.42}$$

At the point (x, z_s, t_s), the disturbance is dominated by a wave having frequency ω_s and wavenumbers $\beta_s, \alpha_m(\omega_s, \beta_s)$. The envelope of its amplitude has an approximate Gaussian shape with respect to the local coordinates and time $t - t_s$. The amplitude maximum is expressed as

$$q(\omega_s, \beta_s, x) = C_{recept} C_{disp} \mathrm{e}^{N(x_0, x)}, \tag{3.43}$$

$$C_{recept} = r_p^2 |D_m(\omega_s, \beta_s) q_m(x, \beta_s, \omega_s)|, \tag{3.44}$$

$$C_{disp} = \frac{2}{\pi} |K(\omega_s, \beta_s)|, \tag{3.45}$$

$$N(x_0, x) = -\int_{x_0}^{x} \alpha_{mi}(x, \beta_s, \omega_s)\, \mathrm{d}x, \tag{3.46}$$

where the coefficient C_{disp} characterizes dispersion of the wavepacket associated with mode m.

If the particle hits the body surface at a point lying in the vicinity of the lower neutral branch, the wavepacket starts to grow just downstream from the excitation region. Hereafter we focus on this most effective case in which x_0 corresponds to the upstream neutral point of mode m at $\beta = \beta_s$ and $\omega = \omega_s$.

Because the coefficient (3.45) and the N factor (3.46) do not depend on receptivity, they are calculated first using the following procedure: (i) by solving the local eigenvalue problem and seeking $\omega_{max}, \beta_{max}$ at which the growth rate $\sigma_m = -\alpha_{mi}$ is maximal, obtain the distributions $\omega_{max}(x)$, $\beta_{max}(x)$ and $\alpha_m(x, \omega_{max}, \beta_{max})$; (ii) from these distributions identify an appropriate set of frequencies $\omega_1, \ldots, \omega_M$ for further analysis; (iii) for a fixed frequency ω_k, determine β_k from the conditions $\beta_k = \beta_{max}(x)$ and $\omega_k = \omega_{max}(x)$; (iv) with β_k fixed, compute the distributions $\alpha_m(x, \omega_k, \beta_k)$, $\alpha_m(x, \omega_k \pm \Delta\omega, \beta_k)$ and calculate $N(x_k, \beta_k, \omega_k) = \int_{x_{0k}}^{x_k} \sigma_m(x, \beta_k, \omega_k)\,\mathrm{d}x$ and the derivative $N_\omega = \int_{x_{0k}}^{x_k} (\partial\sigma_m/\partial\omega)(x, \beta_k, \omega_k)\,\mathrm{d}x$, where x_{0k} is the upstream neutral point and $\partial\sigma_m/\partial\omega$ is calculated using central differences; (v) using the Newton method determine the point x_k at which $N_\omega = 0$, which gives the maximal versus ωN factor at $x = x_k$; (vi) perform steps iv and v at $\beta_k \pm \Delta\beta$ and compute the derivative N_β using central differences; (vii) using the Newton method seek β_{ks} at which the derivative $N_\beta = 0$ and calculate $N(x_{ks}, \beta_{ks}, \omega_k)$ which is maximal versus ω and β at $x = x_{ks}$ and frequency $\omega = \omega_k$, and because $N(x, \omega, \beta) = -S_i(x, \omega, \beta)$, this maximum corresponds to the conditions (3.41) where $\omega_s = \omega_k$ and $\beta_s = \beta_{ks}$; (viii) using central differences calculate the second derivatives $S_{\omega\omega}$, $S_{\beta\beta}$ and $S_{\omega\beta}$; (ix) compute the coefficient (3.40) and the dispersion factor (3.45).

Computations of the receptivity coefficient C_{recept} for different parameters of particles (radius, density etc.) are performed at the neutral point $x = x_{0k}$ for each frequency ω_k and corresponding wavenumber β_{ks}. In (3.44) the coefficient D_m is calculated using (3.35) and q_m is calculated using the eigenfunction $\boldsymbol{A}_m$. The inner product $\langle\cdot,\cdot\rangle$ and the integral in (3.35) are computed numerically in the boundary layer, $0 < y < y_e$, and analytically in the outer flow region, $y_e \leqslant y < \infty$, using asymptotic expressions for the integrands.

Note that the foregoing analysis is valid if the average distance between particles passing through the boundary layer is much larger than the boundary-layer thickness, while it is much smaller than the body length. The first restriction indicates that particles generate wavepackets which interfere only weakly with each other, i.e. the downstream evolution of the wavepackets generated by different particles can be treated independently. The second restriction indicates that there are enough particles to form a transition onset line, which is more or less smooth in the body length scale.

If the concentration of particles is so high that the distance between their trajectories is of the order of the disturbance wavelength and/or the time interval between their strikes is of the order of the instability period, then a resonant excitation of instability may cause a significant increase of the disturbance amplitude. This case needs special consideration.

In the framework of the amplitude method (Mack 1977), the transition onset is associated with the point x_{tr}, where the instability amplitude (3.43) reaches a threshold value $q(x_{tr}) = q_{tr}$. For the TS-dominated transition, the transition onset point is estimated by assuming that at $x = x_{tr}$ the maximal versus y mass-flux amplitude is $q_{tr} \approx 5\,\%$. This assumption is based on the experimental observations (Kosinov *et al.* 1994; Ermolaev, Kosinov & Semionov 1996; Kosinov, Maslov & Semionov 1997) as well as the DNS (Laible, Mayer & Fasel 2008; Mayer, Von Terzi & Fasel 2011) of unstable wavepackets in supersonic boundary layers. Note that in accord with the amplitude method the transition onset point weakly (as log) depends on q_{tr}, and the foregoing rough-order estimate of q_{tr} is acceptable for transition predictions. More accurate evaluation of the threshold amplitude can be performed using the asymptotic theory of nonlinear breakdown (for example, Cowley & Wu 1993; Leib & Lee 1995;

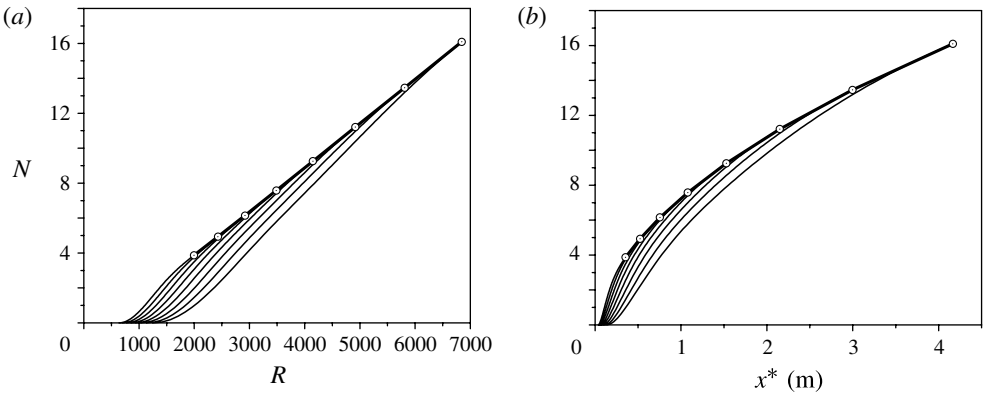

FIGURE 2. N-factors versus R (a) and versus $\boldsymbol{x}^*$ (b). Each curve corresponds to amplification of a TS wave of frequency ω^* and wavenumber β^*, at which N is maximal at a point shown by a corresponding circle. The thick line shows the envelope of lines $N(\omega^*, \beta^*)$.

Wu 2004). The asymptotic theory provides lumped dimensionless parameters, which can be used for capturing the dependence of the critical amplitude on the basic flow parameters such as Mach number, Reynolds number and the wall temperature ratio.

4. Numerical examples

As an example, we consider a sharp wedge of half-angle $\theta_w = 14^\circ$ flying at altitude $H^* = 20$ km, Mach number $M_1 = 4$ and zero angle of attack. Based upon 1976 US Standard Atmosphere, at this altitude the ambient temperature $T_1^* = 216.65$ K, pressure $P_1^* = 5529$ N m^{-2}, density $\rho_1^* = 0.0889$ kg m^{-3}, kinematic viscosity $\nu_1^* = 1.599 \times 10^{-4}$ m^2 s^{-1} and speed of sound $a_1^* = 295.07$ m s^{-1}. The unit Reynolds number based on the speed of sound is $Re_{1a} = a_1^*/\nu_1^* = 1.8455 \times 10^6$ m^{-1}. Air is treated as a perfect gas with the specific heat ratio $\gamma = 1.4$ and Prandtl number $Pr = 0.72$. Under these conditions the inviscid theory predicts the following flow parameters at the upper boundary-layer edge (behind the wedge-induced oblique shock): $M_2 = 3.0$, $T_2^* = 324.86$ K, $Re_1 = U_2^*/\nu_2^* = 11.255 \times 10^6$ m^{-1}, and the stagnation temperature is $T_0^* = 909.6$ K. All stability and receptivity computations were performed for the adiabatic wall temperature

$$T_w^* = T_{ad}^* \approx \left(1 + \sqrt{Pr}\frac{\gamma - 1}{2}M_2^2\right) T_2^* = 821 \text{ K}. \tag{4.1}$$

The viscosity coefficient was calculated using the Sutherland formula with constant 110.4 K. The second viscosity is zero. In the case considered, transition is associated with three-dimensional TS waves – the first mode in accordance with the terminology of Mack (1969).

4.1. *TS wavepackets*

We start with the analysis of TS wavepacket characteristics. Figure 2(a,b) shows the amplification factor distributions $N(R)$ and $N(x^*)$ as well as their envelopes (thick lines with circles), where $R = \sqrt{U_2^* x^*/\nu_2^*}$ is the local Reynolds number. These stability

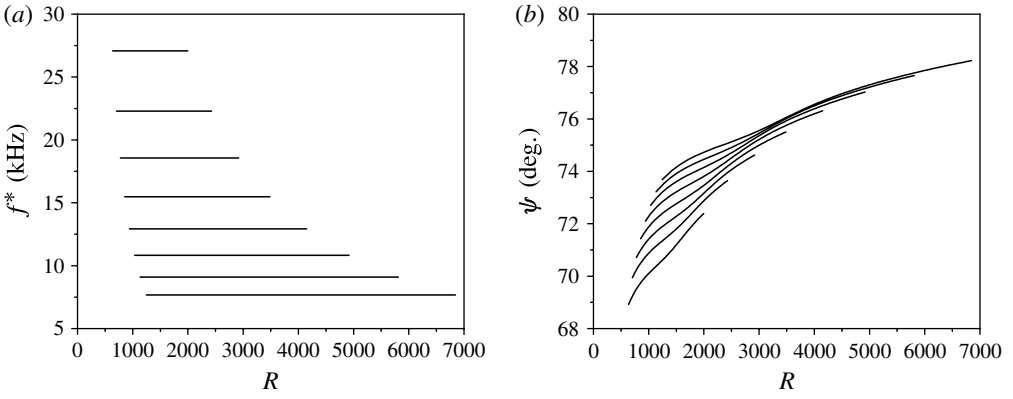

FIGURE 3. Frequencies (a) and the wave-front angles (b) of TS waves for the amplification lines shown in figure 2.

computations are performed in the local parallel approximation, with the mean flow calculated using the compressible Blasius solution. The envelope of $N(R)$ (figure 2a) is almost a straight line which is typical for the boundary-layer flow of zero pressure gradient. The neutral points of unstable waves are close to the wedge leading edge (figure 2b). For example, the line corresponding to $N \approx 9$ at $x^* \approx 143$ cm starts from the neutral point $x_0^* \approx 8$ cm ($x_0^*/x^* \approx 5.6\,\%$). In this most receptive region, very small particles can reach the wedge surface and cross the boundary layer with approximately constant relative velocity (see § 4.2).

The dimensional frequencies for each amplification line are shown in figure 3(a). These frequencies are calculated using the relation $f^* = FU_2^* Re_1/2\pi$, where F is the frequency parameter (in the case considered $U_2^* = 1.084 \times 10^3$ m s^{-1}). Because the longitudinal wavenumber $\alpha_{TS,r}$ depends on the streamwise coordinate, the front angle $\psi = \arctan(\beta/\alpha_{TS,r})$ changes with R at fixed f^* and β^*. The distributions of $\psi(R)$ related to each amplification line are shown in figure 3(b). The appreciable increase of this angle with R indicates that the assumption of $\psi = $ const, which is commonly used in computations of the amplification factor (Malik 1990) may lead to significant errors. Figure 4(a) shows that the TS phase speeds $c_{TS} = \omega/\alpha_{TS,r}$ increase with R. However, their values at the final stations are nearly the same for all the amplification lines ($c_{TS} \approx 0.65$). The dimensional growth rates $\sigma_{TS}^* = -\alpha_{TS,i}^*$ are shown in figure 4(b). Their dependence on R is typical for TS waves in the compressible Blasius boundary layer at supersonic speeds.

As shown in figure 5, the dispersion factor C_{disp} decreases with x^*. It varies from 3×10^{-5} related to the first amplification line (see figure 2b) to 3.5×10^{-6} related to the last line. Small values of C_{disp} indicate that dispersion and selective amplification of TS waves are quite large. This leads to significant reduction of the final amplitude of the TS wavepacket. Note that the dispersion versus frequency is an order of magnitude larger than that versus the lateral wavenumber, $|S_{\omega\omega}/S_{\beta\beta}| \approx 20$.

Hereafter the TS wavepacket is characterized by the mass-flux disturbance $q = (\rho u)'$. The corresponding eigenfunctions

$$q_{TS} = |A_{TS,1} + (\gamma M_e^2 A_{TS,4} - A_{TS,5}/T)U|/T, \tag{4.2}$$

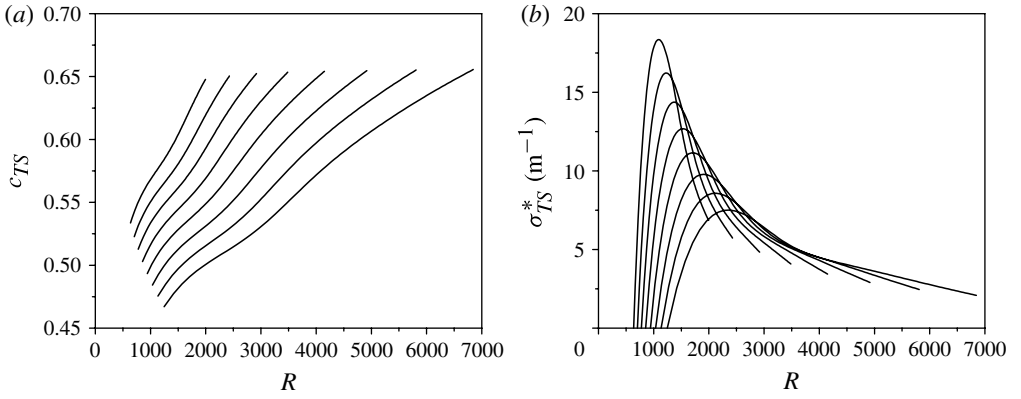

FIGURE 4. Phase speeds c_{TS} (*a*) and dimensional growth rates σ^*_{TS} (*b*) of TS waves for the amplification lines shown in figure 2.

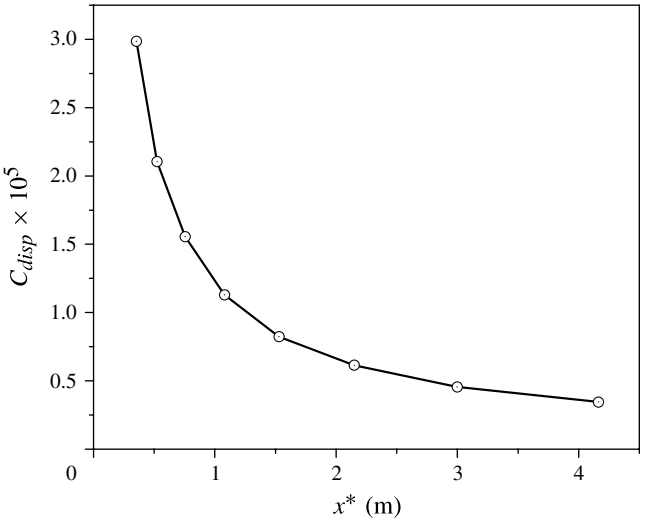

FIGURE 5. Dispersion factor versus x^*; symbols correspond to the circles in figure 2.

which are referenced to their maximum values, are shown in figure 6 at the seven final x-stations. The maximum locus y^*_m increases with x^* owing to the boundary-layer growth. It is close to the critical point where the TS phase speed equals the mean-flow speed.

4.2. *Particle dynamics*

Consider particles of density $\rho^*_p = 1$ g cm^{-3} close to the water density. Equations (2.4)–(2.7) are integrated numerically using the fourth-order Runge–Kutta scheme. In these computations the particle temperature equals the local gas temperature $T_p = T$, i.e. the particle is in thermal equilibrium with the ambient gas and it does not induce a local heat source or sink. Computing the particle trajectories from different initial points located just behind the wedge-induced shock, we obtain

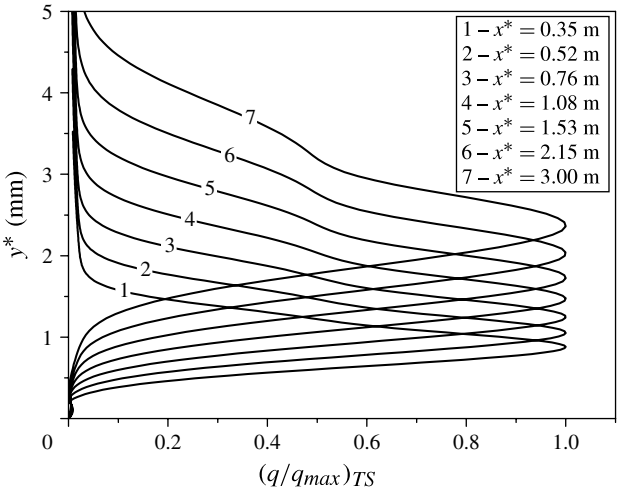

FIGURE 6. The mass-flux eigenfunctions $q_{TS}(y^*)$ at the seven final x-stations corresponding to the circles in figure 2*b*.

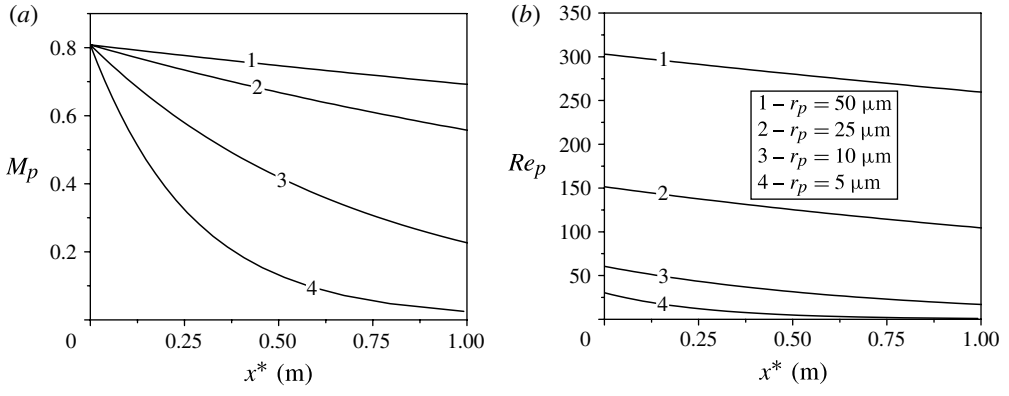

FIGURE 7. Relative Mach number (*a*) and relative Reynolds number (*b*) at the upper boundary-layer edge for particles of density $\rho_p^* = 1$ g cm^{-3} and different radii r_p^*.

streamwise distributions of the particle dynamic parameters at the upper boundary-layer edge. For example, figure 7(*a,b*) shows distributions of the relative Mach number $M_p = |\boldsymbol{u}_p^* - \boldsymbol{u}_2^*|/a_2^*$ and the relative Reynolds number $Re_p = 2r_p^*|\boldsymbol{u}_p^* - \boldsymbol{u}_2^*|/\nu_2^*$ for particles of radii $r_p^* = 5$, 10, 25 and 50 μm. These particles pass through the boundary layer with appreciable subsonic speed in the region $x^* < 0.25$ m (figure 7*a*) containing the neutral points of TS waves (figure 2*b*). The relative Reynolds number Re_p is less than 300 (figure 7*b*) which is adequate for the correlation of Crowe (1967) for the drag coefficient. The relative velocity of a small particle (for example, line 4 for $r_p^* = 5$ μm) quickly decreases with the downstream distance. Ultimately a particle of radius less than 2 μm does not reach the wedge surface for $x^* \geqslant 0.25$ m (not shown here). Further analysis is performed for particulates of radii from 5 to 50 μm.

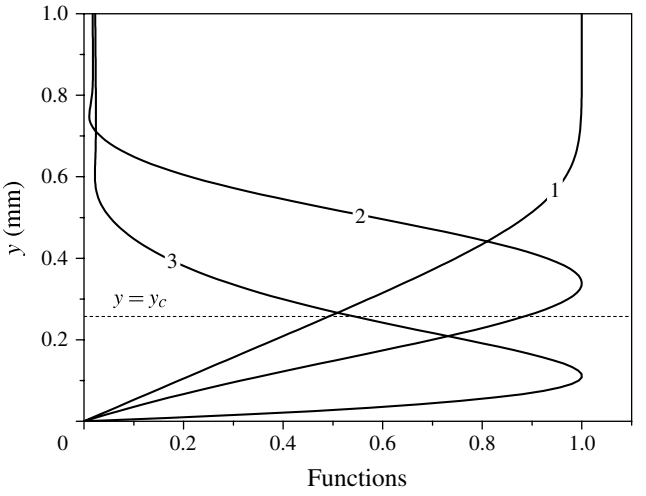

FIGURE 8. The mean velocity profile (line 1), the modulus of the TS eigenfunction for the x-velocity component (line 2), the modulus of normalized receptivity function $\phi(y)$ (line 3) and the critical-layer level $y_c : U(y_c) = c_r$ (dashed line).

4.3. *Receptivity and transition onset*

Consider particles of 50 μm radius and density $\rho_p^* = 1$ g cm^{-3}. To get insight into the receptivity mechanism we focus on the disturbance of frequency 12.9 kHz, which has the neutral point $x_0^* \approx 7.9$ cm ($R_0 \approx 940.5$) and the amplification factor $N \approx 9.25$ (see figure 2). Figure 8 shows the mean velocity profile $U(y)$ (line 1) and the modulus of the TS eigenfunction for the x-velocity component $|A_{TS,1}|$ (line 2) which is normalized by its maximal value. The modulus of the normalized local receptivity function $\phi(y) = |\varphi(y)|/|\varphi|_{max}$, where φ is given by (3.36), is shown by the line 3. The critical-layer level $y_c : U(y_c) = c_{TS}$ is shown by the dashed line. As expected, the maximum of $|A_{TS,1}|$ is observed near the critical point y_c. Because the particle relative velocity is maximal on the wall, the most receptive region is shifted from the critical level toward the wall. Outside the boundary layer, where the TS eigenfunction decays exponentially, the receptivity function is negligibly small. Therefore particulates, which do not reach the boundary layer, are not involved in the direct excitation mechanism considered herein. However such particles generate acoustic waves in the inviscid shock layer. These waves radiate the boundary layer and can excite TS waves. Such an indirect receptivity process, which may be important for very small and/or light particles, needs special consideration.

As shown in figure 9, the receptivity coefficient C_{recept} decreases with the neutral point x_0^*. Its value varies from 4.2 relevant to the first amplification line to 1.8 relevant to the last line. Although receptivity to the particle strike is quite high, dispersion of the initially strong TS wavepacket leads to its significant attenuation associated with the small multiplier C_{disp} (see figure 5).

Figure 10 shows the distributions of the final amplitude $q(R)$ and the envelope $N(R)$ of amplification factors $N(R, \omega, \beta)$. This envelope corresponds to the thick line with circles in figure 2(*a*). Using the transition onset criterion $q_{tr} = 5\,\%$, we obtain $R_{tr} = 3315$ that corresponds to the transition onset Reynolds number

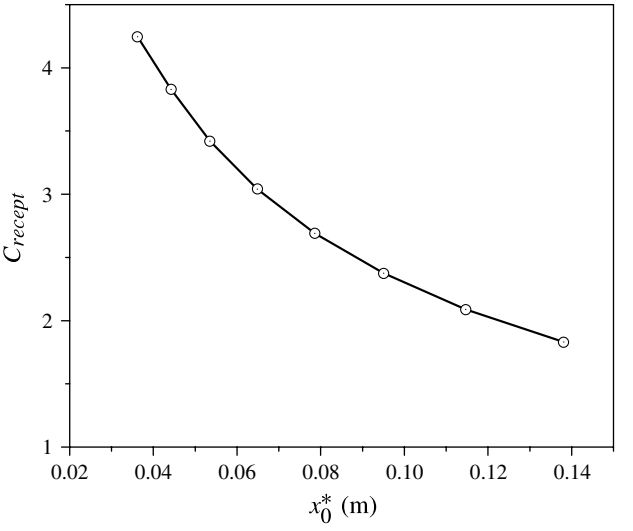

FIGURE 9. Receptivity coefficient versus the neutral point x_0^*. The circles correspond to the initial points of the amplification lines shown in figure 2(*b*).

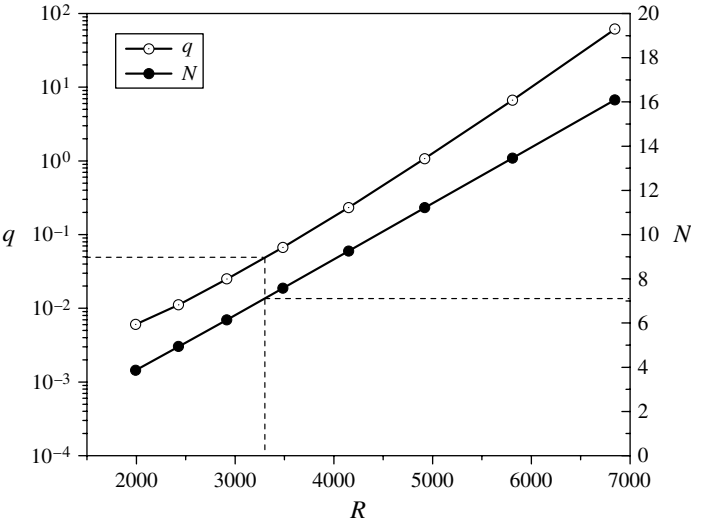

FIGURE 10. Distributions of the final amplitude $q(R)$ (line with open circles) and the N-factor envelope $N(R)$ (line with black circles). The dashed lines show the threshold amplitude $q_{tr} = 5\,\%$ and corresponding values of R_{tr} and N_{tr}.

$Re_{tr} = R_{tr}^2 \approx 11 \times 10^6$ and the amplification factor $N_{tr} \approx 7.1$. These quantities are marked by the dashed lines.

4.4. *Effects of the particle radius, density and temperature*

The functions $q(R)$ computed for different particle radii are shown in figure 11. The particle density is $\rho_p^* = 1$ g cm^{-3}. Using the transition onset criterion $q_{tr} = 5\,\%$ (the

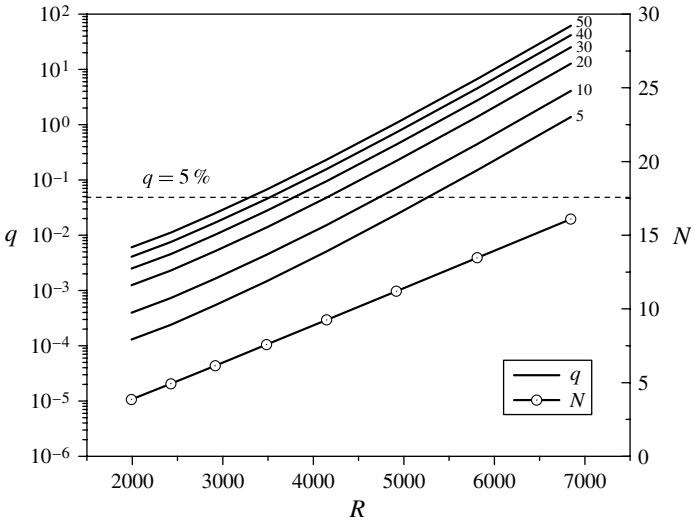

FIGURE 11. Distributions $q(R)$ at different radii r_p^* (given in μm near each line), and the N-factor envelope.

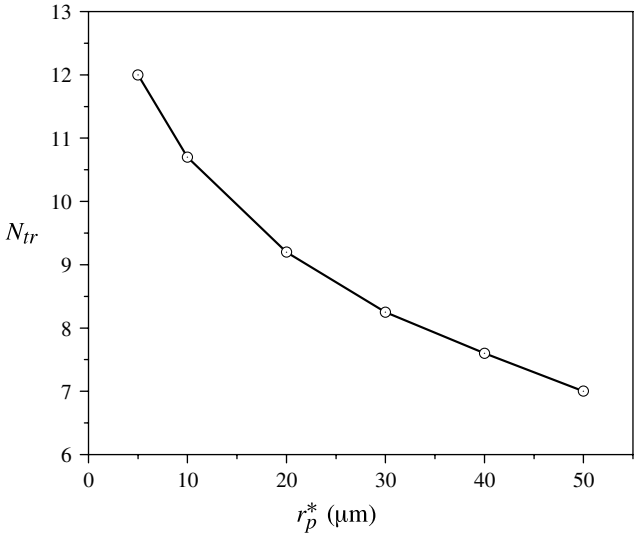

FIGURE 12. The transition onset N-factor versus the particle radius.

horizontal dashed line) we obtain the distributions of N_{tr} and the transition onset Reynolds number Re_{tr} versus the particle radius r_p^* (figures 12 and 13, respectively). As expected, both Re_{tr} and N_{tr} decrease with r_p^*. For the commonly used empirical value $N_{tr} = 10$, the particle radius is estimated as $r_p^* \approx 15$ μm.

Computations for particulates of radius $r_p^* = 20$ μm and density ρ_p^* from 1 to 8 g cm^{-3} show that the particle density has a negligible effect on the receptivity coefficient (figure 14). For smaller particles, this effect is more pronounced but

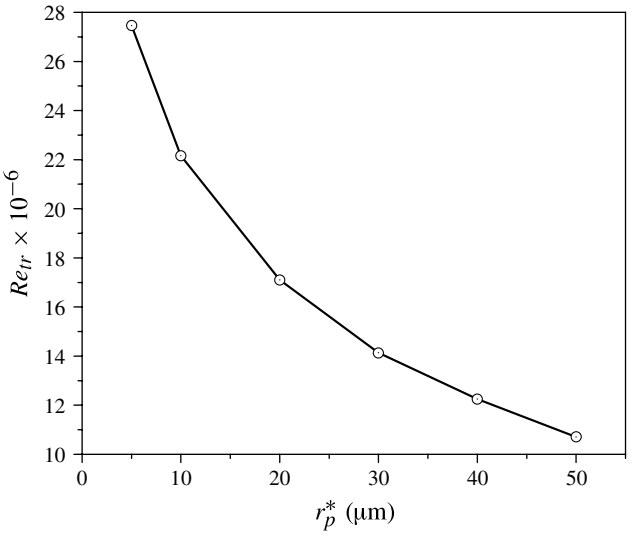

FIGURE 13. The transition onset Reynolds number versus the particle radius.

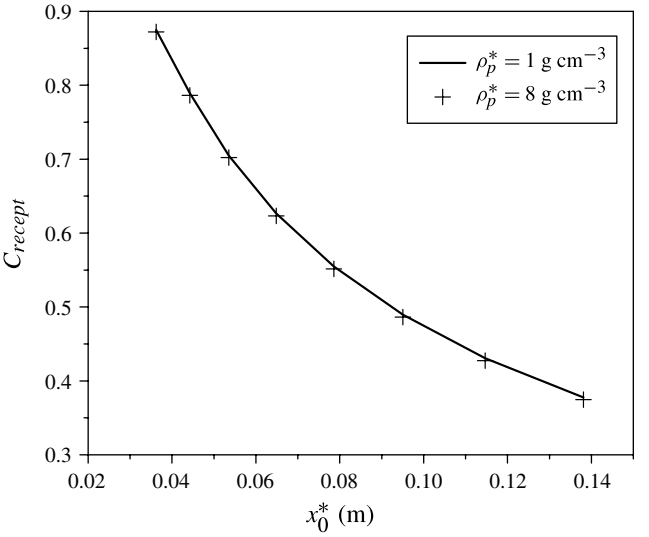

FIGURE 14. Receptivity coefficient for $\rho_p^* = 1$ and 8 g cm^{-3} at $r_p^* = 20$ μm.

still weak. For example, figure 15 shows the receptivity coefficients in the case of $r_p^* = 5$ μm and $\rho_p^* = 1$ and 8 g cm^{-3}. The heavier particle has a smaller effect than the lighter one. However, this difference weakly affects the distribution of $q(R)$ shown in figure 16. Because the particles travel a short distance from the shock to the wall near the wedge nose, where receptivity is significant, they do not have enough time for deceleration. Therefore their relative velocity, which is involved in computations of the receptivity coefficient, does not change much. Such a low sensitivity of the receptivity

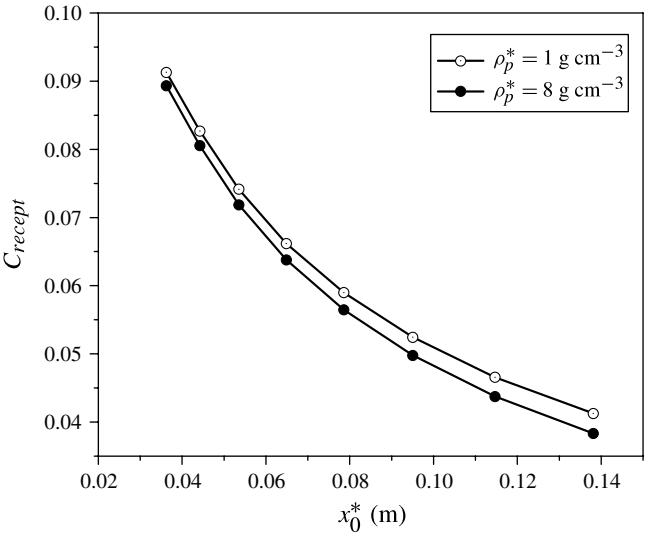

FIGURE 15. Receptivity coefficient for $\rho_p^* = 1$ and 8 g cm^{-3} at $r_p^* = 5$ μm.

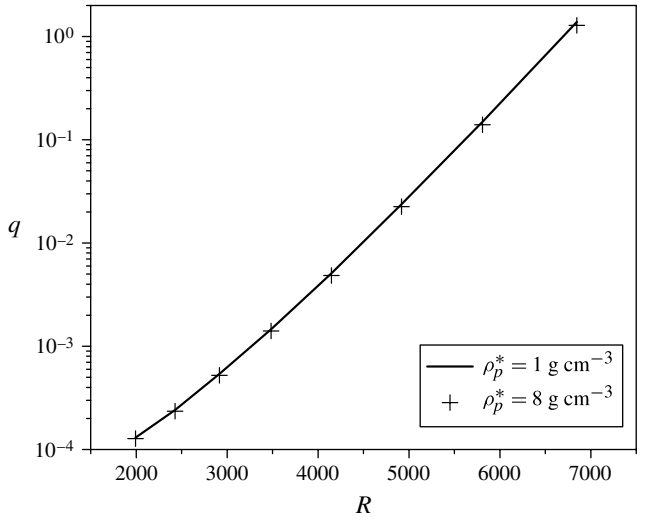

FIGURE 16. Distributions of $q(R)$ for particles of radius $r_p^* = 5$ μm and density $\rho_p^* = 1$ and 8 g cm^{-3}.

mechanism to the particle density allows us to treat practical cases where uncertainty in ρ_p^* is, as a rule, quite large.

The foregoing results were obtained with the assumption that the particle temperature T_p equals the local gas temperature T, i.e. the particle is in thermal equilibrium with the ambient gas flow. In this case the particle-induced heat sink or source is zero and the particle drag force is calculated at $T_p/T = 1$. To evaluate the thermal effect, we consider the opposite case where the particle temperature is frozen

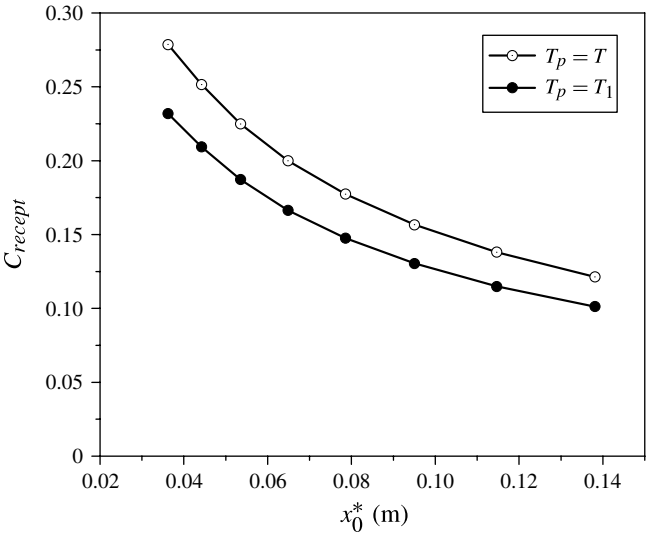

FIGURE 17. Receptivity coefficients for cold (line with black circles) and heated (line with open circles) particles of radius $r_p^* = 10$ μm.

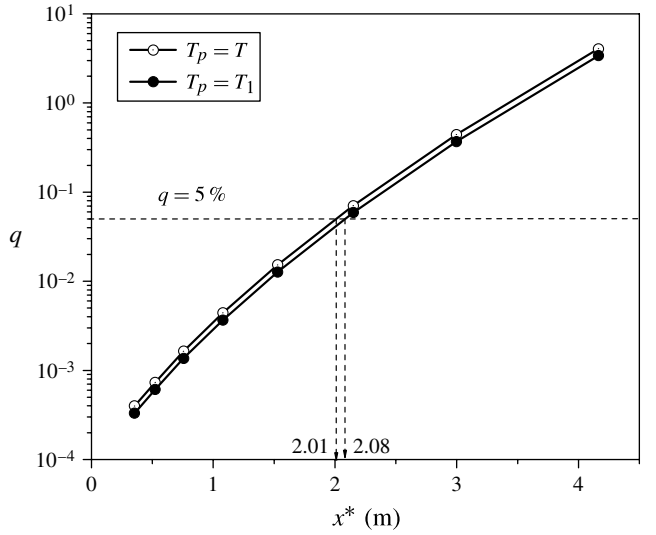

FIGURE 18. Distributions $q(x^*)$ and transition onset points x_{tr}^* predicted for cold (line with black circles) and heated (line with open circles) particles of radius $r_p^* = 10$ μm.

and equals the free-stream temperature. Results of these computations are presented in figures 17 and 18 for the particle of radius $r_p^* = 10$ μm and density $\rho_p^* = 1$ g cm^{-3}. As shown in figure 17, the cold particle with the temperature $T_p = T_1$ has a smaller effect than the thermal-equilibrium (heated) particle with the temperature $T_p = T$. However, the distribution of $q(x^*)$, which is used for prediction of the transition onset, is weakly

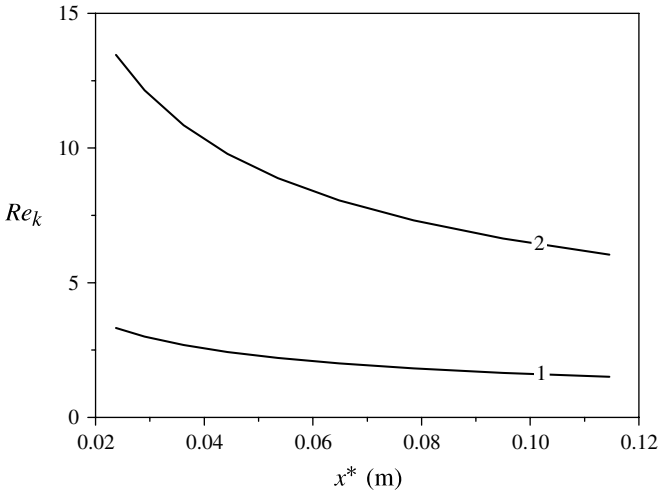

FIGURE 19. Distributions of roughness Reynolds number $Re_k(x^*)$ for particles of radius $r_p^* = 10$ μm (line 1)and 20 μm (line 2).

affected (see figure 18). Namely, the transition onset point is $x_{tr}^* = 201$ cm for the heated particle and $x_{tr}^* = 208$ cm for the cold particle, so that the relative difference $\Delta x_{tr}^*/x_{tr}^* \approx 3.5\,\%$ is small.

The low sensitivity of the receptivity mechanism to the particle temperature can be explained as follows. In the energy equation (3.3), the ratio of the heat source to the drag-power source is of the order of $[r_p PrR(\gamma-1)M_e^2]^{-1} = [r_p^* PrRe_{1e}(\gamma-1)M_e^2]^{-1}$. For the case considered, this ratio is small: it varies from 1.5×10^{-2} to 1.5×10^{-3} on increasing of the particle radius from 5 to 50 μm. This allows us to neglect the heat-source term $\bar{Q}_p$ in (3.3).

Another receptivity source is associated with roughness produced by the particle impact. The roughness size and shape are determined by the physics of collision and essentially depend on the surface structure and the particle matter. Although the collision problem is beyond the scope of this paper, we can perform the following rough-order estimates. If the particle attaches itself to the surface after impact or it rebounds producing a crater, the resulting roughness size and height are assumed to be of the order of the particle diameter $k^* \approx 2r_p^*$. In the absence of a theory for determining the conditions under which this roughness can affect transition, we use empirical correlations (see, for example, Schneider 2008). Probably the best known is the Re_k approach (Reda 2002), which correlates the transition locus with the roughness Reynolds number $Re_k = U^*(k^*)\rho^*(k^*)k^*/\mu^*(k^*)$. Figure 19 shows that distributions of $Re_k(x^*)$ for particles of $r_p^* = 10$ and 20 μm are below the value $Re_k = 25$ which is commonly used as a conservative criterion for aerodynamically smooth surfaces (Schneider 2008). Roughness with $Re_k < 25$ is unlikely to affect the transition process unless there is a mechanism for amplifying the roughness-induced vorticity such as cross-flow (Saric, Reed & White 2003) or Görtler (Saric 1994) instability. Because this mechanism is not present in the wedge configuration considered herein, we conclude that the roughness effect is small compared with receptivity due to the particle passage through the boundary layer in the case of $r_p^* < 20$ μm.

5. Summary

A theoretical model describing excitation of unstable modes by spherical solid particles interacting with a supersonic boundary layer has been developed. The amplitudes of excited unstable waves have been expressed in a compact analytical form. This receptivity solution can be easily incorporated into a stability code in order to predict the downstream propagation of unstable wavepackets. The latter can be related to the Mack first mode typical of supersonic speeds or the Mack second mode typical of hypersonic speeds or the cross-flow instability typical of three-dimensional boundary layers. Receptivity of subsonic boundary layers can be treated as well, if the particle velocity is known at the upper boundary-layer edge.

It should be noted that the analysis is focused on the case where the average distance between particles passing through the boundary layer is much larger than the boundary-layer thickness, while it is much smaller than the distance from the wedge leading edge to the transition onset point. The particles generate wavepackets which interfere only weakly with each other. This case is associated with a relatively small concentration n of particulates. If n is so high that the average distance between particulates is of the order of the boundary-layer thickness, the forcing length scale and frequency become of the order of the wavelength and frequency of instability. Then, a resonant excitation may lead to significant increase of the receptivity coefficient. This case will be analysed in the near future.

Particles also generate acoustic fields (shocklets) and entropy/vorticity wakes, which are expanded into the eigenfunctions of the continuous spectrum (the sum of integrals in (3.24)). Because the latter are orthogonal to the eigenfunctions of the discrete spectrum, they do not directly excite unstable modes except for the special case where an instability of discrete spectrum is synchronized with waves of continuous spectrum (Fedorov & Tumin 2003, 2011). An additional scale-conversion mechanism is required to tune the time and/or length scales of the interacting disturbances. This, as a rule, leads to significant reduction of the receptivity coefficient. Therefore the receptivity mechanism associated with shocklets or entropy/vorticity wakes seems to be essentially weaker than the direct mechanism considered herein. Note that these arguments are not applicable to relatively large particles, which can generate strong vortices and/or shocklets triggering a bypass mechanism.

The foregoing receptivity model needs to be validated. This could be done with the help of DNS and/or experiments. The latter, however, are difficult to set up because it is not clear how to control the particle trajectories and measure the particle-induced disturbances in supersonic wind tunnels. The particles could be launched across the boundary layer from the wall. This technique was developed by Holden (1975) and successfully applied to the problem of the particle–bow-shock interaction on a blunt-body nose at hypersonic speeds. It is also feasible to perform experiments in low-speed wind tunnels, where the problem is much less severe.

The receptivity solutions were plugged in the linear stability code in order to estimate the particle-induced transition onset using the amplitude method of Mack (1977). These estimates were performed for TS-dominated transition on a sharp wedge flying at altitude 20 km, Mach number 4 and zero angle of attack. The dominant excitation of unstable wavepackets occurs near the low branch of the neutral curve. Because the neutral points are close to the wedge leading edge, very small particles (of radius $\sim$5 μm) can reach the wedge surface and cross the boundary layer with appreciable speed. It was found that particulates of radius from 10 to 20 μm and density $\sim$1 g cm^{-3} can cause the transition onset corresponding to the amplification factors $N = 9$–10 which lie in the empirical range $9 \leqslant N \leqslant 12$. This is consistent

with the assumption of Bushnell (1990) that atmospheric particulates may be a major source of transition on aerodynamically smooth surfaces at supersonic speeds.

Rough-order estimates based on the Re_k method showed that roughness produced by particles of $r_p^* < 20$ μm corresponds to $Re_k < 25$. In this case the roughness effect is small compared with the effect of particle passage through the boundary layer. For larger particles or in the presence of cross-flow or Görtler instability, the particle-induced roughness can be a dominant receptivity source, which needs to be studied in detail.

It was found that receptivity weakly depends on the particle density at least for $\rho_p^* \geqslant 1$ g cm^{-3}. The effects associated with heating of particles are also weak and can be neglected in many practical cases. These findings allow us to reduce the number of parameters to be specified. In particular, we can ignore the heat transfer problem for particulates, assuming that particles are in thermal equilibrium with the ambient gas flow. We can also use approximate data for the particle density.

Receptivity and the transition onset essentially depend on the particle radius. Namely, our numerical examples show that the increase of r_p^* from 10 to 20 μm leads to a 20 % reduction of transition onset Reynolds number. Therefore the distribution of free-stream particles versus their radius should be known with sufficiently high accuracy.

It should be noted that the dispersion and selective amplification of TS waves lead to significant reduction of the wavepacket amplitude. In the amplitude method of transition prediction, this factor plays an important role and should be modelled properly.

Acknowledgement

This work is supported by the AFOSR/NASA National Center for Hypersonic Research in laminar–turbulent transition.

Appendix

Introduce the notation:

$$\mathrm{D} = \mathrm{d}/\mathrm{d}y, \quad \mu_s' = \mathrm{d}\mu_s/\mathrm{d}T_s, \quad m = 2(e-1)/3, \quad r = 2(e+2)/3 = m+2$$
$$\text{the ratio of the second viscosity to the first viscosity is } \mu_2/\mu = 2e/3 = 0.8, \tag{A 1}$$

$$\hat{\omega} = \omega - \alpha U_s - \beta W_s, \quad \chi = \left[\frac{R}{\mu_s} - \mathrm{i}r\gamma M_e^2 \hat{\omega}\right]^{-1}. \tag{A 2}$$

Hereafter the subscript 's' denotes mean-flow quantities. Non-zero elements of the matrix $\boldsymbol{H}_0$ are:

$$H_{12} = H_{56} = H_{78} = 1, \quad H_{21} = \alpha^2 + \beta^2 - \mathrm{i}\hat{\omega}\frac{R}{\mu_s T_s}, \quad H_{22} = -\frac{\mathrm{D}\mu_s}{\mu_s}, \tag{A 3a}$$

$$H_{23} = -\mathrm{i}\alpha\left[(m+1)\frac{\mathrm{D}T_s}{T_s} + \frac{\mathrm{D}\mu_s}{\mu_s}\right] + \frac{R\,\mathrm{D}U_s}{\mu_s T_s}, \quad H_{24} = \mathrm{i}\frac{\alpha R}{\mu_s} + (m+1)\gamma M_e^2 \alpha\hat{\omega}, \tag{A 3b}$$

$$H_{25} = -(m+1)\frac{\alpha\hat{\omega}}{T_s} - \frac{\mathrm{D}(\mu_s'\mathrm{D}U_s)}{\mu_s}, \quad H_{26} = -\frac{\mu_s'\mathrm{D}U_s}{\mu_s}, \tag{A 3c}$$

$$H_{31} = -\mathrm{i}\alpha, \quad H_{33} = \frac{\mathrm{D}T_s}{T_s}, \quad H_{34} = \mathrm{i}\gamma M_e^2\hat{\omega}, \quad H_{35} = -\frac{\mathrm{i}\hat{\omega}}{T_s}, \quad H_{37} = -\mathrm{i}\beta, \tag{A 3d}$$

$$H_{41} = -\mathrm{i}\alpha\chi\left(r\frac{\mathrm{D}T_s}{T_s} + 2\frac{\mathrm{D}\mu_s}{\mu_s}\right), \quad H_{42} = -\mathrm{i}\alpha\chi, \tag{A 3e}$$

$$H_{43} = \chi\left[-\alpha^2 - \beta^2 + r\frac{\mathrm{D}\mu_s\mathrm{D}T_s}{\mu_s T_s} + r\frac{\mathrm{D}^2 T_s}{T_s} + \mathrm{i}\frac{R\hat{\omega}}{\mu_s T_s}\right], \tag{A 3f}$$

$$H_{44} = -\mathrm{i}\chi r\gamma M_e^2\left[\alpha\mathrm{D}U_s + \beta\mathrm{D}W_s - \hat{\omega}\left(\frac{\mathrm{D}T_s}{T_s} + \frac{\mathrm{D}\mu_s}{\mu_s}\right)\right], \tag{A 3g}$$

$$H_{45} = \mathrm{i}\chi\left[r\frac{(\alpha\mathrm{D}U_s + \beta\mathrm{D}W_s)}{T_s} + \mu_s'\frac{\alpha\mathrm{D}U_s + \beta\mathrm{D}W_s}{\mu_s} - r\hat{\omega}\frac{\mathrm{D}\mu_s}{\mu_s T_s}\right], \tag{A 3h}$$

$$H_{46} = -\mathrm{i}\chi\hat{\omega}\frac{r}{T_s}, \quad H_{47} = -\mathrm{i}\beta\chi\left(r\frac{\mathrm{D}T_s}{T_s} + 2\frac{\mathrm{D}\mu_s}{\mu_s}\right), \quad H_{48} = -\mathrm{i}\beta\chi, \tag{A 3i}$$

$$\left.\begin{aligned} H_{62} &= -2Pr(\gamma-1)M_e^2\mathrm{D}U_s, \\ H_{63} &= RPr\frac{\mathrm{D}T_s}{\mu_s T_s} - 2\mathrm{i}(\gamma-1)M_e^2 Pr(\alpha\mathrm{D}U_s + \beta\mathrm{D}W_s), \end{aligned}\right\} \tag{A 3j}$$

$$\left.\begin{aligned} H_{64} &= \mathrm{i}RPr\frac{(\gamma-1)M_e^2}{\mu_s}\hat{\omega}, \\ H_{65} &= \alpha^2 + \beta^2 - \mathrm{i}RPr\frac{\hat{\omega}}{\mu_s T_s} - (\gamma-1)M_e^2 Pr \\ &\quad \times\frac{\mu_s'[(\mathrm{D}U_s)^2 + (\mathrm{D}W_s)^2]}{\mu_s} - \frac{\mathrm{D}^2\mu_s}{\mu_s}, \end{aligned}\right\} \tag{A 3k}$$

$$\left.\begin{aligned} H_{66} &= -2\frac{\mathrm{D}\mu_s}{\mu_s}, \quad H_{68} = -2Pr(\gamma-1)M_e^2\mathrm{D}W_s, \\ H_{83} &= \frac{RDW_s}{\mu_s T_s} - \mathrm{i}\beta\left[(m+1)\frac{\mathrm{D}T_s}{T_s} + \frac{\mathrm{D}\mu_s}{\mu_s}\right], \end{aligned}\right\} \tag{A 3l}$$

$$\left.\begin{aligned} H_{84} &= \mathrm{i}\frac{\beta R}{\mu_s} + (m+1)\gamma M_e^2\beta\hat{\omega}, \quad H_{85} = -(m+1)\frac{\beta}{T_s}\hat{\omega} - \frac{\mathrm{D}(\mu_s'\mathrm{D}W_s)}{\mu_s}, \\ H_{86} &= -\frac{\mu_s'\mathrm{D}W_s}{\mu_s}, \quad H_{87} = \alpha^2 + \beta^2 - \mathrm{i}\hat{\omega}\frac{R}{\mu_s T_s}, \quad H_{88} = -\frac{\mathrm{D}\mu_s}{\mu_s}. \end{aligned}\right\} \tag{A 3m}$$

Components of the vector $\boldsymbol{g}(x_p, y, z_p)$ are:

$$\left.\begin{aligned} g_1 = g_3 = g_5 = g_7 = 0, \quad g_2 &= -\bar{F}_{px}(x_p, y, z_p)\frac{R}{\mu_s}, \\ g_4 &= \bar{F}_{py}(x_p, y, z_p) + O(R^{-1}), \end{aligned}\right\} \tag{A 4a}$$

$$\begin{aligned} g_6 = -\frac{RPr}{\mu_s}\{&\sigma\bar{Q}_p(x_p, y, z_p) + (\gamma-1)M_e^2[(U_p(x_p, y, z_p) - U_s)\bar{F}_{px}(x_p, y, z_p) \\ &+ V_p(x_p, y, z_p)\bar{F}_{py}(x_p, y, z_p) + (W_p(x_p, y, z_p) - W_s)\bar{F}_{pz}(x_p, y, z_p)]\} \end{aligned} \tag{A 4b}$$

$$g_8 = -\bar{F}_{pz}(x_p, y, z_p)\frac{R}{\mu_s}, \tag{A 4c}$$

where

$$\bar{F}_{px} = C_D\frac{\rho_s}{2}V_{rel}(U_p - U_s)\pi, \quad \bar{F}_{py} = C_D\frac{\rho_s}{2}V_{rel}V_p\pi, \quad \bar{F}_{pz} = C_D\frac{\rho_s}{2}V_{rel}(W_p - W_s)\pi, \tag{A 5}$$

$$V_{rel} = \sqrt{(U_p - U_s)^2 + V_p^2 + (W_p - W_s)^2}, \tag{A 6}$$

$$\sigma = \frac{1}{r_p Pr R}, \tag{A 7}$$

$$\bar{Q}_p = Nu 2\pi (T_p - T_s). \tag{A 8}$$

REFERENCES

BLACKWELDER, R. F., BROWAND, F. K., FISHER, C. & TANAGUICHI, P. 1992 Initiation of turbulent spots in a laminar boundary layer by rigid particulates. *Bull. Am. Phys. Soc.* **37** (8), 1812.

BUSHNELL, D. 1990 Notes on initial disturbance fields for the transition problem. In *Instability and Transition,* vol. I (ed. M. Y. Hussaini & R. G. Voigt), pp. 217–232. Springer.

CHEN, C. P., GOLAND, Y. & RESHOTKO, E. 1980 Generation rate of turbulent patches in the laminar boundary layer of a submersible. In *Proceedings Symposium on Viscous Drag Reduction* (ed. G. R. Hough), Progress in Astronautics and Aeronautics, vol. 72, pp. 73–89. AIAA.

COWLEY, S. J. & WU, X. 1993 Asymptotic approaches for transition modelling. In *Progress in Transition Modelling*, *AGARD Rep.* 793, chap. 3, pp. 1–38.

CROWE, C. T. 1967 Drag coefficient on particles in a rocket nozzle. *AIAA J.* **5** (5), 1021–1022.

DEEPAK, A. *et al.* 1999 Guide to global aerosol models. *AIAA G*-065-1999.

ERMOLAEV, Y. G., KOSINOV, A. D. & SEMIONOV, N. V. 1996 Experimental investigation of laminar–turbulent transition process in supersonic boundary layer using controlled disturbances. In *Nonlinear Instability and Transition in Three-Dimensional Boundary Layers* (ed. P. W. Duck & P. Hall), pp. 17–26. Kluwer.

FEDOROV, A. V. & KHOKHLOV, A. P. 2002 Receptivity of hypersonic boundary layer to wall disturbances. *Theor. Comput. Fluid Dyn.* **15**, 231–254.

FEDOROV, A. & TUMIN, A. 2003 Initial-value problem for hypersonic boundary-layer flows. *AIAA J.* **41** (3), 379–389.

FEDOROV, A. & TUMIN, A. 2011 High-speed boundary-layer instability: old terminology and a new framework. *AIAA J.* **49** (8), 1647–1657.

HALL, G. R. 1967 Interaction of the wake from bluff bodies with an initially laminar boundary layer. *AIAA J.* **5** (8), 1386–1392.

HEFNER, J. N. & BUSHNELL, D. M. 1979 Application of stability theory to laminar flow control. *AIAA Paper* 1979-1493.

HENDERSON, C. B. 1976 Drag coefficients for spheres in continuum and rarefied flows. *AIAA J.* **14** (6), 707–708.

HOLDEN, M. S. 1975 Studies of transitional flow, unsteady separation phenomena and particle induced augmentation heating on ablated nose tips. *Rep.* AFOSR-TR-76-1066, October.

JAFFE, N. A., OKAMURA, T. T. & SMITH, A. M. O. 1970 Determination of spatial amplification factors and their application to predicting transition. *AIAA J.* **8** (2), 301–308.

KOSINOV, A. D., MASLOV, A. A. & SEMIONOV, N. V. 1997 An experimental study of generation of unstable disturbances on the leading edge of a plate at $M = 2$. *J. Appl. Mech. Tech. Phys.* **38** (1), 45–50.

KOSINOV, A. D., SEMIONOV, N. V., SHEVELKOV, S. G. & ZININ, O. I. 1994 Experiments on the nonlinear instability of supersonic boundary layers. In *Nonlinear Instability of Nonparallel Flows* (ed. D. T. Valentine, S. P. Lin & W. R.C. Philips), pp. 196–205. Springer.

LADD, D. M. & HENDRICKS, E. W. 1985 The effect of background particulates on the delayed transition of a heated 9:1 ellipsoid. *Exp. Fluids* **3**, 113–119.

LAIBLE, A. C., MAYER, C. S. J. & FASEL, H. F. 2008 Numerical investigation of supersonic transition for a circular cone at Mach 3.5. *AIAA Paper* 2008-4397.

LAUCHLE, G. C., PERTIE, H. L. & STINEBRING, D. R. 1995 Laminar flow performance of a heated body in particle-laden water. *Exp. Fluids* **38**, 305–312.

LEIB, S. J. & LEE, S. S. 1995 Nonlinear evolution of a pair of oblique instability waves in a supersonic boundary layer. *J. Fluid Mech.* **282**, 339–371.

MACK, L. M. 1969 Boundary-layer stability theory. Part B. *Doc.* 900-277. JPL, May.

MACK, L. M. 1977 Transition and laminar instability. *NASA-CP*-153203. JPL (May 15).

MALIK, M. R. 1990 Stability theory for laminar flow control design. In *Viscous Drag Reduction in Boundary Layers* (ed. D. M. Bushnell & J. N. Hefner), Progress in Astronautics and Aeronautics, vol. 123, pp. 3–46. AIAA.

MALIK, M. R. 1997 Boundary-layer transition prediction toolkit. *AIAA Paper* 1997-1904.

MAYER, C. S. J., VON TERZI, D. A. & FASEL, H. F. 2011 Direct numerical simulation of complete transition to turbulence via oblique breakdown at Mach 3. *J. Fluid Mech.* **674**, 5–42.

MORKOVIN, M. V., RESHOTKO, E. & HERBERT, T. 1994 Transition in open flow systems – a reassessment. *Bull. Am. Phys. Soc.* **39** (9), 1–31.

NAYFEH, A. H. 1980 Stability of three-dimensional boundary layers. *AIAA J.* **18** (4), 406–416.

REDA, D. C. 2002 Review and synthesis of roughness-dominated transition correlations for reentry applications. *J. Spacecr. Rockets* **39** (2), 161–167.

RESHOTKO, E. 1976 Boundary layer stability and transition. *Annu. Rev. Fluid Mech.* **8**, 311–349.

SAIKI, E. M. & BRINGEN, S. 1996 Spatial numerical simulations of boundary layer transition – effects of a spherical particle. *AIAA Paper* 96-0779.

SALWEN, H. & GROSCH, C. E. 1981 The continuous spectrum of the Orr–Sommerfeld equation. Part 2. Eigenfunction expansion. *J. Fluid Mech.* **104**, 445–465.

SARIC, W. S. 1994 Görtler vortices. *Annu. Rev. Fluid Mech.* **26**, 379–409.

SARIC, W. S., REED, H. L. & WHITE, E. B. 2003 Stability and transition of three-dimensional boundary layers. *Annu. Rev. Fluid Mech.* **35**, 413–440.

SCHNEIDER, S. P. 2008 Effects of roughness on hypersonic boundary-layer transition. *J. Spacecr. Rockets* **45** (2), 193–209.

SMITH, A. M. O. & CLUTTER, D. W. 1959 The smallest height of roughness capable of affecting boundary-layer transition. *J. Aerosp. Sci.* **26**, 229–256.

TANIGUCHI, P. H., BROWAND, F. K. & BLACKWELDER, R. F. 2000 Boundary layer transition due to entry of a small particle. In *Laminar-Turbulent Transition, Proceedings of IUTAM Symposium* (ed. H. Fasel & W. Saric), pp. 199–204. Springer.

TUMIN, A. 2007 Three-dimensional spatial normal modes in compressible boundary layers. *J. Fluid Mech.* **586**, 295–322.

TUMIN, A. M. & FEDOROV, A. V. 1983 Spatial growth of disturbances in a compressible boundary layer. *J. Appl. Mech. Tech. Phys.* **24**, 548–554.

TURCO, R. P. 1992 Upper-atmosphere aerosols: properties and natural cycles, In *The Atmospheric Effects of Stratospheric Aircraft: A First Program Report*, NASA RP-1272, Chap. 3B, pp. 63–91, January.

WU, X. 2004 Non-equilibrium, nonlinear critical layer in laminar–turbulent transition. *Acta Mechanica Sin.* **20** (4), 327–339.

ZHIGULEV, V. N. & TUMIN, A. M. 1987 *Onset of Turbulence*. Nauka.